

Gravitational Wave Duet by Resonating Binary Black Holes with Axion-Like Particles

Jeong Han Kim^{1,*} and Xing-Yu Yang^{2,†}

¹*Department of Physics, Chungbuk National University, Cheongju, Chungbuk 28644, Korea*

²*Quantum Universe Center (QUC), Korea Institute for Advanced Study, Seoul 02455, Republic of Korea*

We leverage gravitational wave observations to explore physics beyond the Standard Model, focusing on axion-like particles (ALPs). This study investigates the resonant effects of ALPs with binary black hole systems, where their oscillatory nature induces time-dependent forces on the black holes. By employing a detailed Fisher matrix analysis, we not only probe a new parameter space for ALPs, characterized by their mass and decay constants, but also assess how these parameters affect gravitational waveforms during black hole mergers. Our approach is distinct as it does not assume interactions of ALPs with photons or nucleons. We demonstrate that as binary black holes spiral inward and lose energy, their orbital frequencies may resonate with those of ALPs, producing distinct oscillatory patterns in gravitational waves detectable by upcoming experiments such as the Laser Interferometer Space Antenna (LISA). This work broadens the potential of gravitational wave astronomy as a tool for dark matter searches, offering a promising avenue for studying elusive components of the universe.

I. INTRODUCTION

Gravitational wave (GW) observations have significantly enhanced our capacity to explore fundamental physics beyond the Standard Model (SM), offering valuable insights into phenomena that cannot be studied through traditional detection methods. These waves are crucial for studying dark matter (DM), which makes up a significant portion of the energy density today. However, its mass and interaction with other particles are still largely unknown [1]. In particular, the GW signals emitted by a black hole binary [2] provide new opportunities to probe DM surrounding a black hole.

This study uses the oscillatory nature of light bosonic DM, which induces metric perturbations and generates distinct patterns in the GWs from binary black hole mergers. Such variations appear as distinct patterns in the waveform, particularly alterations in the frequency and phase of the GWs. These changes can be identified by observatories such as LISA [3], Taiji [4], Tianqin [5], and Deci-hertz Interferometer Gravitational Wave Observatory (DECIGO) [6]. ALPs with mass m and decay constant f_a , hypothesized as light bosonic DM, are especially notable candidates in this pursuit. ALPs are initially inspired by the QCD axion, which was proposed to address the strong CP problem [7–10]. Unlike the QCD axion, ALPs are not directly associated with solving this issue and could exhibit a broader spectrum of masses and coupling constants [11–19].

Prior studies have indicated that GWs could potentially reveal these particles through a black hole super-radiance [20–23], axion-mediated forces and radiations in binary neutron stars [24, 25], scalar field emissions caused by its interaction with gravity [26], frequency modulations [27] and phase deviations [28] as GWs transverse

oscillating scalar fields, dynamical frictions [29–32], and deviations in the speed of GWs [33].

Building on previous studies using pulsar timing arrays that have shown resonant amplification of binary pulsar orbital frequencies caused by ultra-light DM [34–36], we now extend these insights to explore similar resonant interactions within binary black hole systems. As the binary black hole system loses energy and spirals inward, its growing orbital frequency periodically oscillates with the oscillation frequencies of ALPs. These instances of resonance alter the gravitational waveforms, as the frequency of binary black holes sweeps through various harmonics. Observatories like LISA could detect oscillatory patterns in gravitational waveforms, potentially indicating the presence of ultra-light DM as well as shedding new light on ALPs. By using a detailed Fisher matrix analysis, we show that our approach enables exploration across an extensive area of the parameter space for m and f_a , thus greatly expanding the scope of ALPs searches.

Unlike most previous approaches, our method does not presuppose interactions of ALPs with photons or nucleons. This approach is especially important in situations where conventional methods fall short, such as when ALPs exhibit non-existent couplings to the SM particles. By concentrating only on the gravitational interaction between ALPs and black holes, we open a distinctive opportunity to study these elusive particles. This method stands as one of solutions in what could be considered a “nightmare scenario” for ALP detection, where traditional interaction pathways are too faint to be effective.

Our paper is structured as follows. Section II introduces a simplified model of ALPs, and examines how they can cause oscillations in the spacetime metric. Section III then describes the evolution of a binary black hole system under the influence of oscillating ALPs, explaining how these interactions alter black hole dynamics. Section IV presents our main results from the gravitational signal analysis, shedding light on the ALPs parameter space which future experiments such as LISA can probe. This section also discusses the accuracy of ALPs param-

* jeonghan.kim@cbu.ac.kr

† Corresponding author: xingyuyang@kias.re.kr

eter estimation achievable through a Fisher matrix analysis. Finally, Section V concludes with a discussion on the implications of our findings and potential directions for future research.

II. ALPS-INDUCED OSCILLATIONS IN SPACETIME

We consider a generic real scalar field Φ with the following action

$$S = \int d^4x \sqrt{-g} \left[\frac{M_{\text{pl}}}{2} R - \frac{1}{2} g^{\mu\nu} \partial_\mu \Phi \partial_\nu \Phi - V(\Phi) \right], \quad (1)$$

where $M_{\text{pl}} = \sqrt{1/8\pi G}$ denotes a reduced Planck mass¹, R is the Ricci scalar, $V(\Phi) = \frac{1}{2} m^2 \Phi^2 + \frac{\lambda}{4!} \Phi^4$ represents the potential of the scalar field with its mass m and a quartic self-coupling constant λ . The potential of ALPs is typically characterized by a periodic form

$$V(\Phi) = m^2 f_a^2 \left(1 - \cos \frac{\Phi}{f_a} \right). \quad (2)$$

For small field values, the expression simplifies to approximately $V(\Phi) \approx \frac{1}{2} m^2 \Phi^2 - \frac{1}{4!} \frac{m^2}{f_a^2} \Phi^4$. Consequently, a negative quartic self-coupling constant arises, denoted as $\lambda = -m^2/f_a^2$. The volume factor $d^4x \sqrt{-g}$ is invariant under a general coordinate transformation where $g = \det(g_{\mu\nu})$ denotes the determinant of the Friedmann–Lemaître–Robertson–Walker (FLRW) metric in Newtonian gauge

$$ds^2 = -[1 + 2\phi(t, \vec{x})] dt^2 + [1 - 2\psi(t, \vec{x})] \delta_{ij} dx^i dx^j. \quad (3)$$

Here, $\phi(t, \vec{x})$ and $\psi(t, \vec{x})$ represent scalar perturbations in spacetime.

A key attribute of ALPs is their capability to create a stable configuration, referred to as a soliton, made up of condensed fields with random phases. This configuration results in an interference pattern of wave packets in space, each approximately the size of the de Broglie wavelength, $\lambda_{\text{dB}} = 2\pi/(mv)$ where v is a virial velocity. Within each wave packet, the fields exhibit coherent oscillations. Collectively, these ALPs behave like a single macroscopic fluid. In the non-relativistic limit, this behavior is effectively captured by the general form of the ALPs [37, 38]

$$\Phi(t, \vec{x}) = \Phi_0(\vec{x}) \cos(\omega_a t + \Upsilon(\vec{x})), \quad (4)$$

where $\Phi_0(\vec{x})$ and $\Upsilon(\vec{x})$ are functions that exhibit slow changes in positions, and $\omega_a = m(1 + \frac{\lambda}{16m^2} \Phi_0^2)$ denotes the angular frequency of ALPs².

The corresponding energy-momentum tensor reads

$$T^\mu{}_\nu = g^{\mu\alpha} \partial_\alpha \Phi \partial_\nu \Phi - \delta^\mu{}_\nu \left(\frac{1}{2} g^{\rho\sigma} \partial_\rho \Phi \partial_\sigma \Phi + V(\Phi) \right). \quad (5)$$

The energy density for the ALPs can be derived from the time-time component of the energy-momentum tensor. Taking the average of the ALPs density during a time period of density oscillation, $2\pi/\omega_a$, yields³

$$\bar{\rho}_{\text{DM}} = \frac{1}{2} m^2 \Phi_0^2 + \frac{3\lambda}{64} \Phi_0^4 + \frac{\lambda^2}{1024 m^2} \Phi_0^6, \quad (6)$$

where we have neglected the terms with spatial derivatives in Φ . However, solitons cannot sustain densities beyond a certain threshold, as they become unstable and collapse (detailed stability criteria are provided in Appendix A). In our study, we have selected benchmark values for $\bar{\rho}_{\text{DM}}$ ranging from 10^{16} to $10^{20} M_\odot/\text{pc}^3$, which are compatible with the stability criteria.

By utilizing Eq.(6), we are able to determine the amplitude, $\Phi_0^2 = \bar{\rho}_{\text{DM}} \Lambda / m^2$, where Λ is a dimensionless function of $\hat{\lambda}$ defined in Eq.(B1), and $\hat{\lambda} \equiv \lambda \bar{\rho}_{\text{DM}} / m^4$ is a dimensionless parameter defined within the interval $\hat{\lambda} \in [-\sqrt{64/27}, 0)$.

The pressure can be computed from the spatial components of the the energy-momentum tensor

$$P_{\text{DM}} = -\bar{\rho}_{\text{DM}} \left[\Lambda_0 + \Lambda_2 \cos(2\omega_a t + 2\Upsilon) + \Lambda_4 \cos(4\omega_a t + 4\Upsilon) \right], \quad (7)$$

where

$$\Lambda_0 = -\frac{\hat{\lambda}}{64} \Lambda^2 - \frac{\hat{\lambda}^2}{1024} \Lambda^3, \quad (8a)$$

$$\Lambda_2 = \frac{1}{2} \Lambda + \frac{5\hat{\lambda}}{96} \Lambda^2 + \frac{\hat{\lambda}^2}{1024} \Lambda^3, \quad (8b)$$

$$\Lambda_4 = \frac{\hat{\lambda}}{192} \Lambda^2. \quad (8c)$$

Thus, the ALPs pressure consists of a constant part Λ_0 , along with time-varying terms Λ_2 and Λ_4 with oscillating at frequencies of $2\omega_a$ and $4\omega_a$ respectively. These dimensionless parameters are confined within the range $-1 \leq \Lambda_{0,2,4} \leq 1$. As $\hat{\lambda}$ approaches zero, Λ_2 dominates over Λ_0 and Λ_4 . On the other hand, as $\hat{\lambda}$ approaches its lower limit, the magnitudes of Λ_0 and Λ_4 increase, but Λ_2 remains the dominant term throughout (see Appendix B for more details).

¹ We set $c = \hbar = 1$ in Section II and related Appendices for the notational brevity.

² While the self-gravity of ALPs contributes to their angular frequency, our main focus is on how their self-interaction impacts this frequency. To simplify the discussion, we will neglect the contribution from self-gravity.

³ Noting that the density profile of ALPs varies with the distance from the center. A detailed examination of this density profile requires solving the Schrödinger–Poisson equations to accurately determine the distribution of ALPs, which we intend to address in future work.

To study oscillations induced by ALPs in spacetime, we calculate perturbed Einstein equations

$$\nabla^2 \psi = 4\pi G \rho_{\text{DM}}, \quad (9)$$

$$\ddot{\psi} + \frac{1}{3} \nabla^2 (\phi - \psi) = 4\pi G P_{\text{DM}}. \quad (10)$$

Neglecting the spatial gradients and using Eq.(10), we obtain (see Appendix C for more details)

$$\ddot{\psi} = -4\pi G \bar{\rho}_{\text{DM}} \left[\Lambda_2 \cos(2\omega_a t + 2\Upsilon) + \Lambda_4 \cos(4\omega_a t + 4\Upsilon) \right]. \quad (11)$$

This equation describes the change in the metric perturbation over time at frequencies $2\omega_a$ and $4\omega_a$, influenced by the ALPs pressure.

III. BINARY BLACK HOLES

We explore a binary system consisting of black holes with masses M_1 and M_2 , surrounded by a cloud of ALPs. The metric perturbation induced by ALPs in Eq.(11) can generate an additional force between the black holes. The Fermi normal coordinates provide a convenient way to express the geodesic deviation equations for the binary [34, 39]

$$\ddot{\mathbf{r}} = -F_{\text{DM}} \hat{\mathbf{r}}, \quad (12)$$

where \mathbf{r} is a vector connecting the two bodies, and $F_{\text{DM}} = \ddot{\psi} r$ denotes the exerted force. In our analysis, at a separation distance of approximately $\mathcal{O}(100)$ Schwarzschild radii between the binary black holes, we assume that the ALPs density is locally homogeneous and isotropic relative to the barycenter of the binary system, leading to a radially exerted force. This additional force perturbs the Keplerian orbit of the binary system [40]

$$\frac{da}{dt} = -2\sqrt{\frac{a^3}{GM}} \frac{e}{\sqrt{1-e^2}} \sin(\varphi - \varphi_p) F_{\text{DM}}, \quad (13a)$$

$$\frac{de}{dt} = -\sqrt{\frac{a}{GM}} \sqrt{1-e^2} \sin(\varphi - \varphi_p) F_{\text{DM}}, \quad (13b)$$

$$\frac{d\varphi_p}{dt} = \sqrt{\frac{a}{GM}} \frac{\sqrt{1-e^2}}{e} \cos(\varphi - \varphi_p) F_{\text{DM}}, \quad (13c)$$

$$\frac{d\varphi}{dt} = \sqrt{\frac{GM}{a^3}} \frac{[1 + e \cos(\varphi - \varphi_p)]^2}{(1-e^2)^{3/2}}, \quad (13d)$$

where $M \equiv M_1 + M_2$ is the total mass of the binary, a stands for the semimajor axis, e denotes the eccentricity, φ is the orbital angle, and φ_p is the longitude of the pericenter. Eq.(13a) demonstrates that a non-zero value of e increases the effect of the additional force on the rate of change in a . Similarly, Eq.(13b) shows that the rate of change in e is influenced by this external force.

In addition, the emission of GWs results in the loss of

energy and angular momentum of the binary [41]

$$\left\langle \frac{da}{dt} \right\rangle = -\frac{64G^3 \mu M^2}{5c^5 a^3 (1-e^2)^{7/2}} \left(1 + \frac{73}{24} e^2 + \frac{37}{96} e^4 \right), \quad (14a)$$

$$\left\langle \frac{de}{dt} \right\rangle = -\frac{304G^3 \mu M^2 e}{15c^5 a^4 (1-e^2)^{5/2}} \left(1 + \frac{121}{304} e^2 \right), \quad (14b)$$

where $\langle \dots \rangle$ denotes the average taken over a single orbital period⁴.

To solve the orbital evolution as described in Eqs.(13-14), it is convenient to define the following dimensionless quantities

$$\begin{aligned} \alpha &\equiv \frac{a}{R_*}, \quad \tau \equiv \frac{tc}{R_*}, \quad \eta \equiv \frac{\mu}{M}, \\ \zeta &\equiv \frac{4\pi G \bar{\rho}_{\text{DM}} R_*^2}{c^2}, \quad \nu \equiv \Omega/\omega, \end{aligned} \quad (15)$$

where $R_* \equiv GM/c^2$ represents half of the Schwarzschild radius of a binary, $\mu \equiv M_1 M_2 / M$ is a reduced mass, $\omega = \sqrt{GM/a^3}$ denotes an orbital frequency of a binary system, and $\Omega = 2\omega_a$ is related to the oscillation frequency of ALPs.

Applying Fourier decomposition to the orbital elements and averaging these values over the orbital period, $T = 2\pi/\omega$, the orbital equations simplify to (refer to Appendix D for detailed explanations)

$$\begin{aligned} \left\langle \frac{d\alpha}{d\tau} \right\rangle &= \zeta \alpha^{5/2} \frac{2e}{\sqrt{1-e^2}} \left[\Lambda_2 \sin(\pi\nu + \gamma) \mathcal{S}(\nu, e) \right. \\ &\quad \left. + \Lambda_4 \sin(2\pi\nu + 2\gamma) \mathcal{S}(2\nu, e) \right] \\ &\quad - \frac{64\eta}{5\alpha^3 (1-e^2)^{7/2}} \left(1 + \frac{73}{24} e^2 + \frac{37}{96} e^4 \right), \end{aligned} \quad (16a)$$

$$\begin{aligned} \left\langle \frac{de}{d\tau} \right\rangle &= \zeta \alpha^{3/2} \sqrt{1-e^2} \left[\Lambda_2 \sin(\pi\nu + \gamma) \mathcal{S}(\nu, e) \right. \\ &\quad \left. + \Lambda_4 \sin(2\pi\nu + 2\gamma) \mathcal{S}(2\nu, e) \right] \\ &\quad - \frac{304\eta e}{15\alpha^4 (1-e^2)^{5/2}} \left(1 + \frac{121}{304} e^2 \right), \end{aligned} \quad (16b)$$

$$\begin{aligned} \left\langle \frac{d\varphi_p}{d\tau} \right\rangle &= -\zeta \alpha^{3/2} \frac{\sqrt{1-e^2}}{e} \left[\Lambda_2 \cos(\pi\nu + \gamma) \mathcal{C}(\nu, e) \right. \\ &\quad \left. + \Lambda_4 \cos(2\pi\nu + 2\gamma) \mathcal{C}(2\nu, e) \right], \end{aligned} \quad (16c)$$

$$\left\langle \frac{d\varphi}{d\tau} \right\rangle = \alpha^{-3/2}, \quad (16d)$$

⁴ When stellar black holes move through a DM environment, they would typically experience dynamical friction. Nonetheless, to concentrate on the main aspect of resonant effects, we will omit the impacts of dynamical friction and halo feedback from our discussion, saving it for future work.

where $\gamma = \Omega t_p + 2\Upsilon$. Generally, it is possible to choose the initial time and coordinates in such a way that $t_p = 0$ and $\varphi = \varphi_p = 0$, as well as $\Upsilon = 0$.

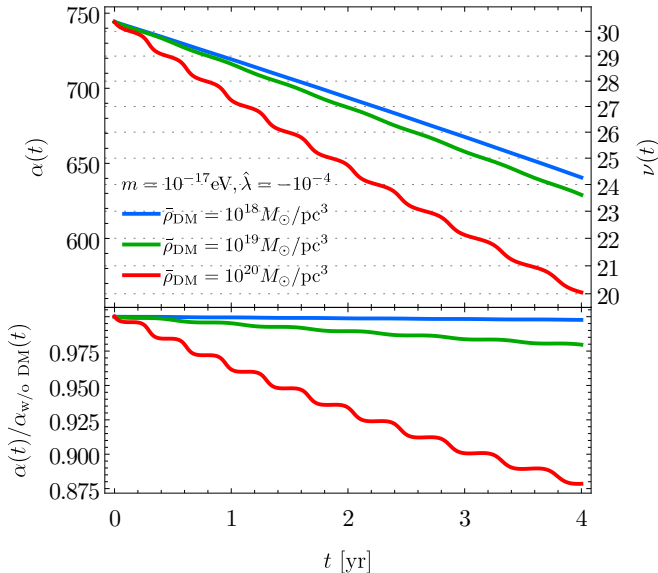


FIG. 1. The time evolution of the dimensionless semimajor axis α for an equal-mass binary system characterized by a total mass $M = 10^4 M_\odot$, an initial orbital frequency $\omega_0 = 10^{-3}$ Hz, and an initial eccentricity $e_0 = 0.5$. Benchmark ALPs parameters include $m = 10^{-17}$ eV and $\hat{\lambda} = -10^{-4}$ with average ALPs densities (blue, green, and red lines) given by $\bar{\rho}_{\text{DM}} = \{10^{18}, 10^{19}, 10^{20}\} M_\odot/\text{pc}^3$ respectively.

Figure 1 shows how the dimensionless semimajor axis α changes over time for a binary system with equal masses. This system has a total mass $M = 10^4 M_\odot$, an initial orbital frequency of $\omega_0 = 10^{-3}$ Hz, and an initial eccentricity of $e_0 = 0.5$. We take the benchmark ALPs parameters, $m = 10^{-17}$ eV and $\hat{\lambda} = -10^{-4}$ with average ALPs densities given by $\bar{\rho}_{\text{DM}} = \{10^{18}, 10^{19}, 10^{20}\} M_\odot/\text{pc}^3$ respectively. The lower subfigure displays the ratio of α to the vacuum scenario in the absence of ALPs cloud near the binary system. As α decreases over time, causing ω to increase, the ratio ν consequently decreases, as indicated by the additional y -axis on the right side of the plot. Notably, when the ALPs density is high, for instance $\bar{\rho}_{\text{DM}} = 10^{20} M_\odot/\text{pc}^3$, the plot reveals distinctive oscillatory features in α , characterized by periodic dips occurring at specific intervals of ν . This behavior highlights the dynamic interaction between the gravitational effects of the binary system and the surrounding ALPs environment. The time evolution of other orbital elements, e , φ_p , and φ , is detailed in Appendix D.

IV. GRAVITATIONAL WAVES

The waveform of GWs originating from the inspiral of a binary system is described by [41, 42]

$$h_+(t) =_{\text{ret}} \frac{1}{1-e^2} \frac{4(GM_c)^{5/3} \omega^{2/3}}{d_L c^4} \left\{ \frac{1+\cos^2 \iota}{2} \cos(2\varphi-2\beta) + \frac{e}{4} \sin^2 \iota \left[\cos(\varphi-\varphi_p) + e \right] + \frac{e}{8} (1+\cos^2 \iota) \left[5 \cos(\varphi-2\beta+\varphi_p) + \cos(3\varphi-2\beta-\varphi_p) + 2e \cos(2\beta-2\varphi_p) \right] \right\}, \quad (17a)$$

$$h_\times(t) =_{\text{ret}} \frac{1}{1-e^2} \frac{4(GM_c)^{5/3} \omega^{2/3}}{d_L c^4} \left\{ \cos \iota \sin(2\varphi-2\beta) + \frac{e}{4} \cos \iota \left[5 \sin(\varphi-2\beta+\varphi_p) + \sin(3\varphi-2\beta-\varphi_p) - 2e \sin(2\beta-2\varphi_p) \right] \right\}, \quad (17b)$$

where ‘ $=_{\text{ret}}$ ’ indicates that the right-hand side is computed at retarded time. The symbol $M_c = \mu^{3/5} M^{2/5}$ represents the chirp mass, d_L stands for the luminosity distance to a source, ι denotes the angle between the orbital angular momentum axis of a binary and the direction to a detector, and β represents the azimuthal component of the inclination angle.

Taking the Fourier transformation of Eq.(17a) and Eq.(17b), we can obtain the amplitude spectral density of GWs in the frequency domain as shown in Figure 2. The red (black) line corresponds to the binary system with (without) ALPs clouds. Each broad peak corresponds to the n -th harmonic in the Fourier decomposition of the Keplerian motion. These peaks occur at $f_n = n\omega_0/2\pi$ with $n \geq 1$. In contrast to the vacuum scenario, the binary system surrounded by ALPs clouds exhibits a residual oscillatory pattern at each peak location. These non-trivial oscillations occur due to the oscillatory behavior of the orbital elements, as explained in Section III. In the future, identifying oscillatory patterns in GWs may indicate the existence of ALPs. A detailed analysis of these GW signals could potentially reveal the mass and coupling constants of ALPs.

LISA operates in a heliocentric orbit and is composed of three spacecraft arranged in an equilateral triangle, with each spacecraft 2.5 million kilometers apart from the others. The constellation’s center of mass, known as the guiding center, moves in a circular orbit 1 AU away from the Sun and lags 20 degrees behind Earth. Using a polar coordinate system centered on the Sun, the strain of gravitational waves at a detector is described by [44]

$$h(t) = h_+(t-\Delta t)F_+(t-\Delta t) + h_\times(t-\Delta t)F_\times(t-\Delta t), \quad (18)$$

where F_+ and F_\times represent the detector response functions, which depend on the latitude θ and longitude ϕ of

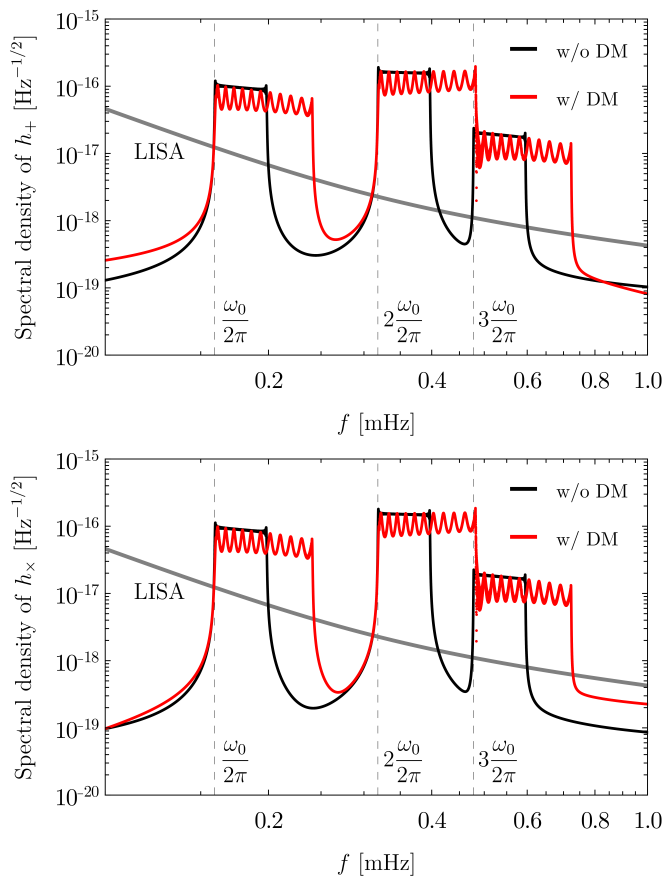


FIG. 2. The amplitude spectral density of GWs with (red line) and without (black line) ALPs clouds around the binary system located at $d_L = 0.1\text{Gpc}$ with orbital inclinations $\iota = \pi/4$ and $\beta = \pi/4$. The binary system and benchmark ALPs parameters are same as those presented in Figure 1, except that the average ALPs density is fixed by $\bar{\rho}_{\text{DM}} = 10^{20} M_\odot/\text{pc}^3$. The gray line represents LISA’s sensitivity curve [43].

the binary, as well as the polarization angle ψ of GWs, and Δt is the time delay between the arrival of GWs at the Sun and their detection.

When the signal-to-noise ratio (SNR) is high, the posterior probability distribution for the source parameters can be approximated as a multivariate Gaussian distribution, centered on the true values. The associated covariance matrix can be determined using the inverse of the Fisher information matrix. For a network of N independent detectors, the Fisher matrix is expressed as

$$\Gamma_{ij} = \left(\frac{\partial \mathbf{d}(f)}{\partial \theta_i}, \frac{\partial \mathbf{d}(f)}{\partial \theta_j} \right)_{\theta = \hat{\theta}}, \quad (19)$$

where \mathbf{d} is given by

$$\mathbf{d}(f) = \left[\frac{\tilde{h}_1(f)}{\sqrt{S_1(f)}}, \frac{\tilde{h}_2(f)}{\sqrt{S_2(f)}}, \dots, \frac{\tilde{h}_N(f)}{\sqrt{S_N(f)}} \right]^T, \quad (20)$$

where θ represents the vector of parameters with its true value denoted by $\hat{\theta}$. In this context, $S_i(f)$ refers to the

noise power spectral density of the i -th detector, and $\tilde{h}_i(f)$ is the Fourier transform of the signal in the time domain. The bracket operator (A, B) for any two functions $A(t)$ and $B(t)$ is defined as

$$(A, B) = 2 \int_{f_{\min}}^{f_{\max}} df \left[\tilde{A}(f) \tilde{B}^*(f) + \tilde{A}^*(f) \tilde{B}(f) \right]. \quad (21)$$

The total SNR is given by $\sqrt{(\mathbf{d}, \mathbf{d})}$.

The root-mean-squared errors for the parameters can be derived from the inverse of the Fisher matrix

$$\sigma_{\theta_i} = \sqrt{(\Gamma^{-1})_{ii}}. \quad (22)$$

In our analysis, θ consists of 14 parameters

$$\theta = \{M, \eta, \omega_0, e_0, \varphi_0, d_L, \iota, \beta, \theta, \phi, \psi; \bar{\rho}_{\text{DM}}, m, \hat{\lambda}\}, \quad (23)$$

where the first 11 parameters are related to the binary black holes and the last 3 parameters are related to the ALPs. The angles $\{\iota, \beta, \theta, \phi, \psi\}$ are each set to $\pi/4$. We adjust the luminosity distance d_L to vary SNR.

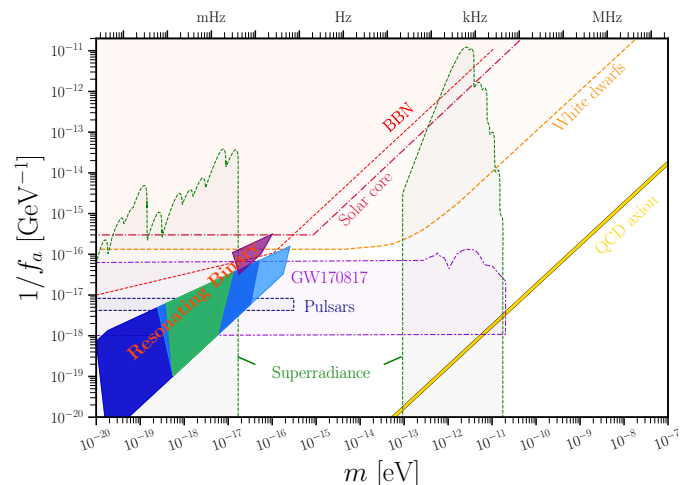


FIG. 3. The detectable regions in the parameter space of $\{m, 1/f_a\}$ for binary systems under different conditions are shown. The reference parameters (highlighted in light blue) involve a binary system with $M = 10^2 M_\odot$, an initial eccentricity $e_0 = 0.5$, and an average ALPs density $\bar{\rho}_{\text{DM}} = 10^{18} M_\odot/\text{pc}^3$. Additional scenarios include a system with a lower initial eccentricity $e_0 = 0.3$ (in green), another with a lower ALPs density $\bar{\rho}_{\text{DM}} = 10^{16} M_\odot/\text{pc}^3$ (in purple), and a binary system with an increased total mass of $M = 10^4 M_\odot$ (in dark blue).

Figure 3 shows the detectable region within the parameter space of $\{m, 1/f_a\}$ for an equal-mass binary system with a total mass of $M = 10^2 M_\odot$ and an initial orbital frequency of $\omega_0 = 10^{-2} \text{Hz}$ (highlighted in light blue), referred to as the reference set of parameters. This region corresponds to relative errors in mass and coupling, σ_m and $\sigma_{\hat{\lambda}}$, to be less than 0.1, while also satisfying the stability requirement for solitons in Eq.(A5). The SNR is assumed to be 100, the initial eccentricity is set

at $e_0 = 0.5$, and the average ALPs density is fixed by $\bar{\rho}_{\text{DM}} = 10^{18} M_{\odot}/\text{pc}^3$. The detection of oscillatory features in GWs through LISA could potentially pinpoint the mass and the coupling constant within the range

$$\begin{aligned} m &\in (2.0 \times 10^{-19}, 2.0 \times 10^{-16}) \text{ eV} , \\ 1/f_a &\in (1.0 \times 10^{-19}, 2.0 \times 10^{-16}) \text{ GeV}^{-1} . \end{aligned} \quad (24)$$

The detectable region from our analysis overlaps with those derived from the superradiance of black holes [45–47], Big Bang Nucleosynthesis (BBN) [48], the solar core [24], white dwarfs [24], GW signals from the neutron star binary GW170817 [49], and pulsar binaries [49] (as referenced in Ref. [50])⁵. Our analysis does not rely on the superradiance and the interactions of ALPs with photons or nucleons. This strategy is essential in situations where superradiance may not occur or ALPs might have weak or nonexistent interactions with the SM particles. Focusing exclusively on the gravitational interactions between ALPs and black holes, we provide an independent method to explore these elusive entities.

To expand the detectable region to lower ALPs mass ranges, we consider a binary system with a larger total mass, $M = 10^4 M_{\odot}$, which possesses a lower initial orbital frequency $\omega_0 = 10^{-3} \text{ Hz}$ (shown in dark blue)⁶. With respect to the reference parameters, additional scenarios include a lower initial eccentricity $e_0 = 0.3$ (shown in dark green) and a smaller higher ALPs density $\bar{\rho}_{\text{DM}} = 10^{16} M_{\odot}/\text{pc}^3$ (shown in dark purple). The detectable region aligns diagonally because the force from ALPs is related to the dimensionless parameter $\hat{\lambda} = -\frac{\bar{\rho}_{\text{DM}}}{m^2 f_a^2}$.

The parameter space that can be identified through resonating black holes can be further extended to higher ALPs mass by considering a binary system with a smaller total mass or a higher initial eccentricity. Investigating much lower values of $1/f_a$ requires a higher value of $\bar{\rho}_{\text{DM}}$.

V. CONCLUSIONS

In this study, we have explored the interactions between ALPs and binary black hole systems, specifically

⁵ Beyond the limits shown, future projections include LIGO’s observations of neutron star and black hole mergers [25], the Piezoaxionic effect [51], and the Cosmic Axion Spin Precession Experiment (CASPER) [52]. The QCD axion is identified by the yellow solid line showing the relationship between mass and coupling.

⁶ This is because the influence of ALPs on orbital dynamics is most pronounced when the ratio $\nu \equiv \Omega/\omega$ is around the order of 10, as indicated by the special function $\mathcal{S}(\nu, e)$ in Eq.(D7) and demonstrated in Figure 7. If ν is excessively high or low, the impact on orbital motion diminishes. To stay within the most sensitive range of ν , if the angular frequency of ALPs $\Omega = 2\omega_a$ is decreased, then the orbital frequency ω of the binary system, must also decrease accordingly.

examining how these particles can influence the dynamics and gravitational waveforms of such systems. We discovered that ALPs can induce time-dependent forces on black holes as they spiral inward, leading to measurable changes in the gravitational waveforms emitted during their mergers. By using a detailed Fisher matrix analysis, we investigated the new ALPs parameter space of $\{m, 1/f_a\}$, and assessed how these parameters can impact the observable GW signals through LISA. This approach expands the range of DM searches, especially in situations where superradiance is absent or ALPs do not interact with the SM particles. This method is applicable to ultra-light bosonic DM with a positive quartic self-coupling, where the instability issue of solitons does not create inaccessible regions, as well as to cases without self-interaction. The implications of our research are significant for future experiments such as LISA, Taiji, Tianqin, and DECIGO, which could detect these unique signals across wide frequency ranges.

As we conclude our discussion, it is important to acknowledge that further exploration is needed to understand the effects of dynamical friction on black holes moving through ALPs environment and halo feedback. We plan to address this topic in subsequent studies. Additional exploration of the ALPs density profile around black holes, which was not covered in our current study, is necessary. For example, while we have used specific benchmark density values, $\bar{\rho}_{\text{DM}}$, a detailed investigation using the Schrödinger-Poisson equations to accurately model the ALPs distribution around black holes is essential and planned for future work.

ACKNOWLEDGMENTS

We appreciate Sergey Sibiryakov and Clifford P. Burgess for the valuable discussions during our visit to McMaster University, where the inspiration for this project began. JHK thanks Han Gil Choi and Chang Sub Shin for useful comments. JHK is supported by the National Research Foundation of Korea grant funded by the Korea government(MSIT) [NRF-2021R1C1C1005076]. XYY is supported in part by the KIAS Individual Grant No. QP090701.

Appendix A: Stability Conditions for Soliton Configurations in ALPs

The negative sign of the self-coupling λ causes ALPs to interact attractively with each other. To form a stable soliton, a quantum pressure is required to counterbalance the attractive forces and gravity. The mass of a stable

soliton cannot exceed a specific threshold [53–55]

$$M_{\text{th}} \simeq 10.2 \frac{m_{\text{pl}}}{|\lambda|^{1/2}} = (1.1 \times 10^8 M_{\odot}) \left(\frac{10^{-18} \text{GeV}^{-1}}{1/f_a} \right) \left(\frac{10^{-18} \text{eV}}{m} \right), \quad (\text{A1})$$

where $m_{\text{pl}} = \sqrt{1/G}$ denotes a Planck mass. Beyond this threshold, the system is predicted to collapse. Figure 4 (dashed lines) displays the threshold masses for the soliton across our parameter space of interest. In this area, solitons reach a higher threshold mass of approximately $10^8 M_{\odot}$ for lower values of m and $1/f_a$. Conversely, the threshold mass decreases to about $10^6 M_{\odot}$ for higher values of m and $1/f_a$.

The radius containing 99% of the mass of the soliton is

$$R_{99} = 5.5 \left(\frac{|a|}{Gm^3} \right)^{1/2}, \quad (\text{A2})$$

where $a = \lambda/(32\pi m)$ denotes a scattering length. This can be expressed in terms of the decay constant and the mass of ALPs

$$R_{99} \simeq (4.3 \times 10^{-5} \text{pc}) \left(\frac{1/f_a}{10^{-18} \text{GeV}^{-1}} \right) \left(\frac{10^{-18} \text{eV}}{m} \right). \quad (\text{A3})$$

Figure 4 (dotted lines) illustrates that for lower m and higher $1/f_a$, the soliton's size reaches approximately $R_{99} \sim 10^{-4} \text{pc}$. Conversely, the soliton shrinks to a smaller size, $R_{99} \sim 10^{-6} \text{pc}$, for larger m and smaller $1/f_a$. Our study focuses on a separation distance of approximately $\mathcal{O}(100)r_s$ between the binary black holes, given the Schwarzschild radius of the binary as $r_s = 2GM/c^2 \sim 10^{-9} \text{pc}$ for $M = 10^4 M_{\odot}$. Therefore, the binary system is situated within the soliton's structure.

The highest central density of the soliton is determined by

$$\rho^* = 0.04 \frac{Gm^4}{a^2}. \quad (\text{A4})$$

This can be expressed as

$$\rho^* = (9.3 \times 10^{21} M_{\odot}/\text{pc}^3) \left(\frac{10^{-18} \text{GeV}^{-1}}{1/f_a} \right)^4 \left(\frac{m}{10^{-18} \text{eV}} \right)^2. \quad (\text{A5})$$

The upper limit of the ALPs density increases with larger values of m and smaller values of $1/f_a$, as depicted in Figure 4 (solid lines). For instance, the red solid line in the plot indicates the density threshold, $\rho^* = 10^{18} M_{\odot}/\text{pc}^3$. Above this threshold, the environment is too dense to support a soliton with average densities of $\bar{\rho}_{\text{DM}} \geq 10^{18} M_{\odot}/\text{pc}^3$.

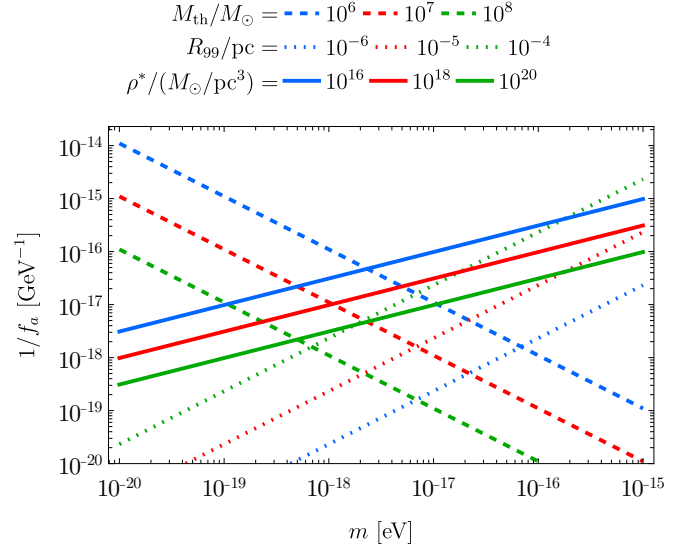


FIG. 4. The threshold mass (dashed), the radius containing 99% of the mass (dotted), and the highest central density (solid lines) of the soliton in the parameter space of $\{m, 1/f_a\}$.

Appendix B: Pressure Modulations in ALPs

Based on Eq.(6), we can obtain the amplitude, $\Phi_0^2 = \bar{\rho}_{\text{DM}} \Lambda / m^2$, where Λ is defined by

$$\Lambda = -\frac{16}{\hat{\lambda}} - \frac{8(-27\hat{\lambda}^4 - 3\sqrt{3}\hat{\lambda}^3\sqrt{-64 + 27\hat{\lambda}^2})^{1/3}}{3\hat{\lambda}^2} - \frac{32}{(-27\hat{\lambda}^4 - 3\sqrt{3}\hat{\lambda}^3\sqrt{-64 + 27\hat{\lambda}^2})^{1/3}}, \quad (\text{B1})$$

where $\hat{\lambda} \equiv \lambda \bar{\rho}_{\text{DM}} / m^4$ denotes a dimensionless parameter defined in the interval $\hat{\lambda} \in [-\sqrt{64/27}, 0)$.

The pressure can be expressed using these parameters as detailed in Eq.(7). Figure 5 illustrates the behavior of the dimensionless parameters Λ_0 , Λ_2 , and Λ_4 defined in Eq.(8) as functions of $\hat{\lambda}$. As $\hat{\lambda}$ approaches zero, Λ_2 clearly dominates over Λ_0 and Λ_4 , indicating that the oscillatory component of the pressure at frequency $2\omega_a$ (associated with Λ_2) is significantly larger than the other components. On the other hand, as $\hat{\lambda}$ approaches its lower limit, the magnitudes of Λ_4 and Λ_0 increase, but the contribution from Λ_2 remains comparatively dominant throughout, suggesting that its impact on the overall pressure modulation is large.

Figure 6 shows the modulation of pressure, normalized by $\bar{\rho}_{\text{DM}}$, as a function of mt . As $\hat{\lambda}$ decreases to its minimum value of $-\sqrt{64/27}$, the angular frequency of ALPs $\omega_a = m(1 + \hat{\lambda}\Lambda/16)$ becomes smaller as illustrated by the blue line. Fisher analysis in Section IV is highly sensitive to changes in pressure based on $\hat{\lambda}$. As the value of $\hat{\lambda}$ approaches its minimum, this sensitivity increases. Conversely, as $\hat{\lambda}$ approaches to zero, the variations in pres-

sure exhibit less fluctuation. The observed trends suggest that the estimation error, $\sigma_{\hat{\lambda}}$, derived from Fisher analysis will be minimized as $\hat{\lambda}$ approaches its lower limit. In other words, this parameter space enables more precise exploration, reducing the relative error and improving the accuracy of parameter measurements.

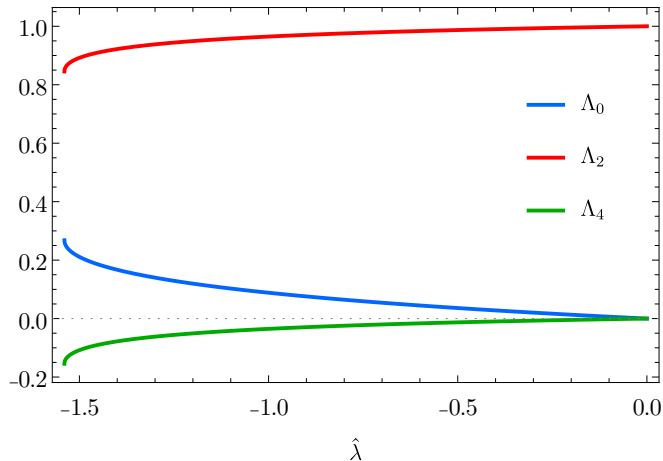


FIG. 5. Variation of the dimensionless pressure components, Λ_0 , Λ_2 , and Λ_4 , defined in Eq.(8) as functions of $\hat{\lambda}$.

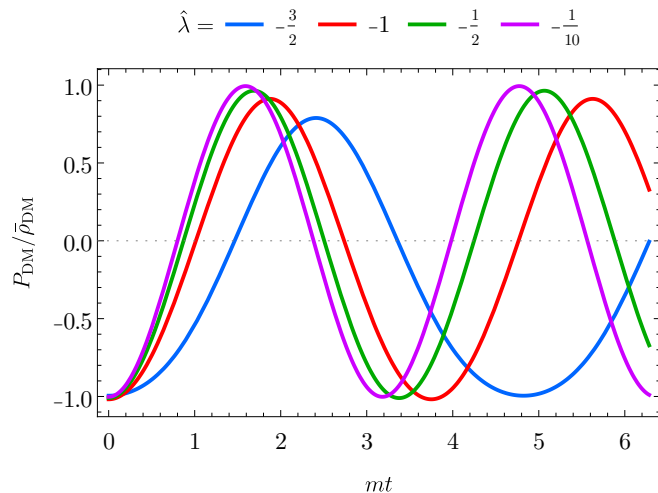


FIG. 6. Pressure modulations in ALPs, normalized by average density $\bar{\rho}_{\text{DM}}$, as a function of mt for different values of $\hat{\lambda}$.

Appendix C: Perturbed Einstein Equations

In this section, we solve the time-time and the space-space component of Einstein Eq.(9) and Eq.(10) respectively, following a similar method as discussed in Ref [56]. We do not consider the time-space component of Einstein equation, $\nabla\psi = 0$, because it gives a trivial result. The gravitational potential ψ consists of the time-

independent components along with parts that oscillate at frequencies of $2\omega_a$ and $4\omega_a$. The proposed form for the solution of ψ is

$$\psi(t, \vec{x}) = \bar{\psi}(\vec{x}) + \tilde{\psi}_2(\vec{x}) \cos(2\omega_a t + 2\Upsilon(\vec{x})) + \tilde{\psi}_4(\vec{x}) \cos(4\omega_a t + 4\Upsilon(\vec{x})), \quad (\text{C1})$$

where $\bar{\psi}(\vec{x})$ denotes a time-independent component, and spatial gradients of $\tilde{\psi}_2(\vec{x})$ and $\tilde{\psi}_4(\vec{x})$ are assumed to be small. Likewise, the same applies for $\phi(t, \vec{x})$. However, as this does not affect the final analysis, we will focus on $\psi(t, \vec{x})$.

Taking time-independent parts from Eq.(9) and taking a Fourier transformation, we find

$$\bar{\psi}(k) = -\frac{4\pi G \bar{\rho}_{\text{DM}}}{k^2}. \quad (\text{C2})$$

The time-independent components of Eq.(10) gives

$$\nabla^2(\bar{\psi} - \bar{\phi}) = 12\pi G \bar{\rho}_{\text{DM}} \Lambda_0, \quad (\text{C3})$$

which indicates that $\bar{\psi} \neq \bar{\phi}$. Neglecting the spatial gradients, The time-dependent components of Eq.(10) gives

$$\tilde{\psi}_2(\vec{x}) = \frac{\pi G \bar{\rho}_{\text{DM}} \Lambda_2}{\omega_a^2}, \quad (\text{C4})$$

$$\tilde{\psi}_4(\vec{x}) = \frac{\pi G \bar{\rho}_{\text{DM}} \Lambda_4}{4\omega_a^2}, \quad (\text{C5})$$

Differentiating ψ with respect to time twice, we have

$$\ddot{\psi} = -4\pi G \bar{\rho}_{\text{DM}} \left[\Lambda_2 \cos(2\omega_a t + 2\Upsilon) + \Lambda_4 \cos(4\omega_a t + 4\Upsilon) \right]. \quad (\text{C6})$$

Appendix D: Averaged Orbital Dynamics

The Kepler's equation is given by [40]

$$u - e \sin u = \omega(t - t_p), \quad (\text{D1})$$

where u denotes an eccentric anomaly and t_p is a time of pericenter passage. Any quantity averaged over a single orbital period $T = 2\pi/\omega$ is formulated as follows

$$\langle \dots \rangle \equiv \int_0^T \frac{dt}{T} (\dots) = \int_0^{2\pi} \frac{d\xi}{2\pi} (\dots), \quad (\text{D2})$$

where $\xi \equiv \omega \tilde{t}$ and $\tilde{t} \equiv t - t_p$.

We consider the Fourier decomposition of Keplerian functions for the following quantities [34, 57]

$$\frac{r}{a} \sin \tilde{\varphi} = \frac{2\sqrt{1-e^2}}{e} \sum_{n=1}^{\infty} \frac{J_n(ne)}{n} \sin(n\omega \tilde{t}), \quad (\text{D3})$$

$$\frac{r}{a} \cos \tilde{\varphi} = -\frac{3e}{2} + 2 \sum_{n=1}^{\infty} \frac{J'_n(ne)}{n} \cos(n\omega \tilde{t}), \quad (\text{D4})$$

where $\tilde{\varphi} \equiv \varphi - \varphi_p$ denotes a true anomaly, $J_n(z)$ is the Bessel function, and $J'_n(z)$ is its derivative with respect to z . Time-averaged quantities can be computed by

$$\begin{aligned} & \left\langle \frac{r}{a} \sin \tilde{\varphi} \cos(\Omega \tilde{t} + \gamma) \right\rangle \\ &= \int_0^{2\pi} \frac{d\xi}{2\pi} \left[\frac{2\sqrt{1-e^2}}{e} \sum_{n=1}^{\infty} \frac{J_n(ne)}{n} \sin(n\xi) \right] \cos(\nu\xi + \gamma) \\ &= \sin(\pi\nu + \gamma) \mathcal{S}(\nu, e), \end{aligned} \quad (\text{D5})$$

and

$$\begin{aligned} & \left\langle \frac{r}{a} \cos \tilde{\varphi} \cos(\Omega \tilde{t} + \gamma) \right\rangle \\ &= \int_0^{2\pi} \frac{d\xi}{2\pi} \left[-\frac{3e}{2} + 2 \sum_{n=1}^{\infty} \frac{J'_n(ne)}{n} \cos(n\xi) \right] \cos(\nu\xi + \gamma) \\ &= \cos(\pi\nu + \gamma) \mathcal{C}(\nu, e), \end{aligned} \quad (\text{D6})$$

where special functions, $\mathcal{S}(\nu, e)$ and $\mathcal{C}(\nu, e)$, are defined by Eq.(D7) and Eq.(D8) respectively.

$$\begin{aligned} \mathcal{S}(\nu, e) &= \frac{2\sqrt{1-e^2} \sin(\pi\nu)}{\pi e} \sum_{n=1}^{\infty} \frac{J_n(ne)}{n^2 - \nu^2} \\ &= \begin{cases} 0, & \nu = 0 \\ \frac{(-1)^{\nu-1} \sqrt{1-e^2}}{2\nu} [J_{\nu-1}(\nu e) + J_{\nu+1}(\nu e)], & \nu = 1, 2, \dots \\ \frac{\sqrt{1-e^2}}{2\pi \sin(\pi\nu)} \times \\ \int_0^{2\pi} du (1 - e \cos u) \sin u \cos[\nu(u - e \sin u)], & \nu \notin \mathbb{Z} \end{cases} \end{aligned} \quad (\text{D7})$$

$$\begin{aligned} \mathcal{C}(\nu, e) &= -\frac{\sin(\pi\nu)}{\pi\nu} \left[\frac{3e}{2} + 2 \sum_{n=1}^{\infty} \frac{J'_n(ne) \nu^2}{(n^2 - \nu^2)n} \right] \\ &= \begin{cases} -\frac{3e}{2}, & \nu = 0 \\ \frac{(-1)^\nu}{2\nu} [J_{\nu-1}(\nu e) - J_{\nu+1}(\nu e)], & \nu = 1, 2, \dots \\ \frac{1}{2\pi \sin(\pi\nu)} \times \\ \int_0^{2\pi} du (1 - e \cos u) (\cos u - e) \sin[\nu(u - e \sin u)], & \nu \notin \mathbb{Z} \end{cases} \end{aligned} \quad (\text{D8})$$

Figure 7 shows the evolution of Eq.(D5) and Eq.(D6) as a function of ν for various values of eccentricities, $e = 0.1, 0.5, 0.9$. As the separation between the binary components decreases over time, causing ω to increase, the ratio ν consequently diminishes as the binary nears coalescence. As ν decreases over time, both functions exhibit periodic oscillations. Notably, peaks occur periodically within intervals of ν .

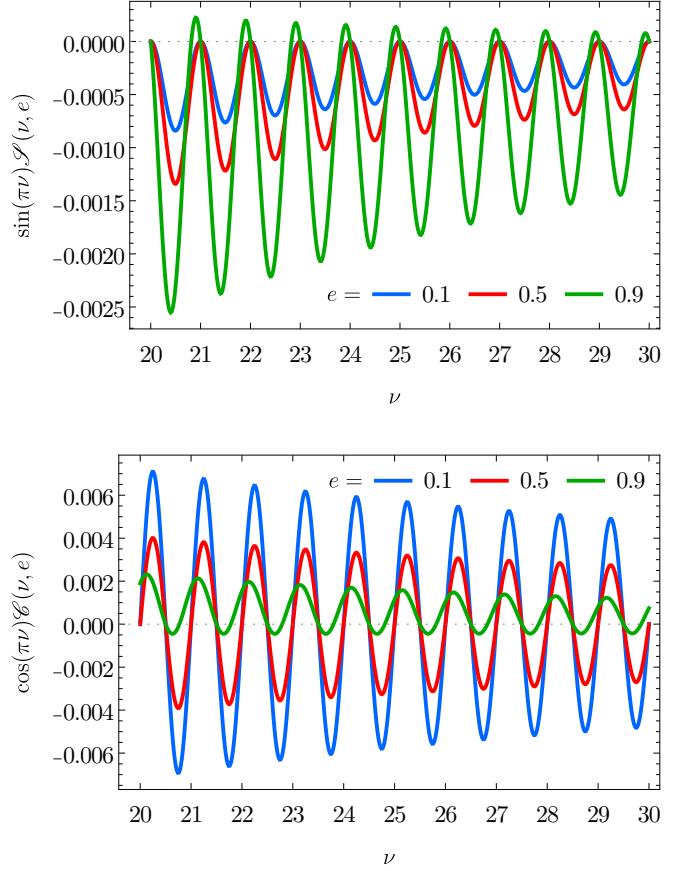


FIG. 7. The evolution of time-averaged quantities in Eq.(D5) (top) and Eq.(D6) (bottom) as a function of ν for various values of $e = 0.1, 0.5, 0.9$. As ν decreases over time, both functions exhibit periodic oscillations. Notably, peaks occur periodically within intervals of ν .

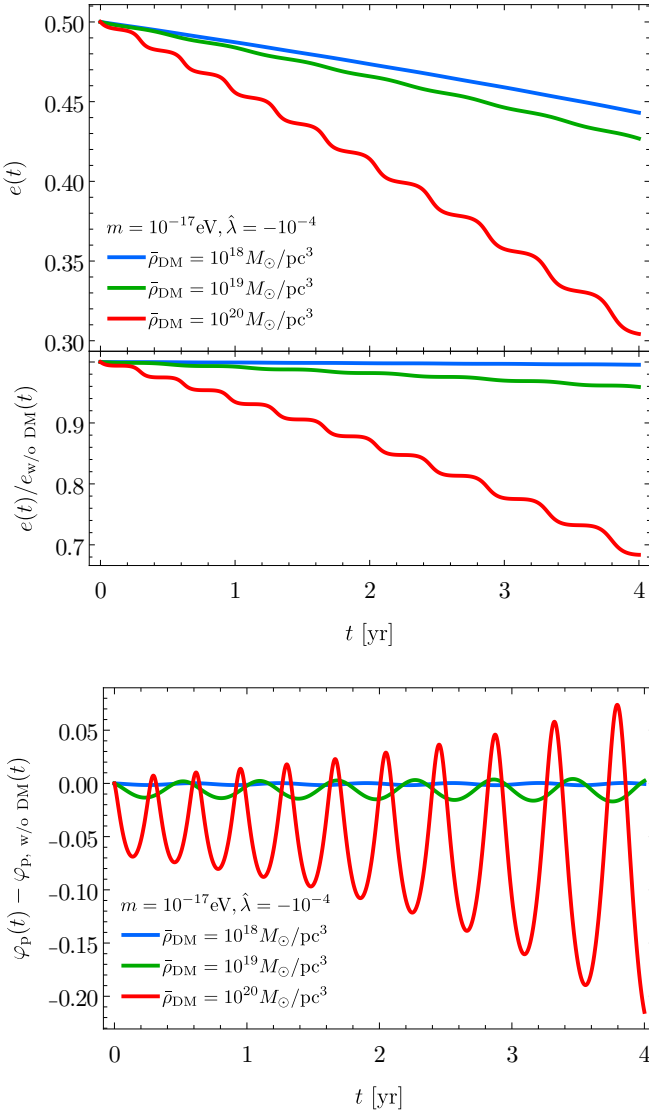


FIG. 8. The time evolution of the eccentricity e and the longitude of the pericenter φ_p for a binary system characterized by a total mass $M = 10^4 M_\odot$, an initial orbital frequency $\omega_0 = 10^{-3} \text{Hz}$, and an initial eccentricity $e_0 = 0.5$. Benchmark ALPs parameters are $m = 10^{-17} \text{eV}$ and $\hat{\lambda} = -10^{-4}$.

In Eq.(16a), the function in Eq.(D5) plays a crucial role in influencing the dynamics of the dimensionless semi-major axis α and the eccentricity e due to interactions with ALPs as shown in Figure 1 and Figure 8 (top panel) respectively. As time progresses and ν decreases, the Eq.(D5) oscillates and mainly becomes a negative value. This contributes to a resonant force that acts to reduce the value of α and e , at the points where ν roughly reaches integer values.

In Eq.(16c), the function in Eq.(D6) is important for determining the variations in the longitude of the pericenter φ_p , due to the resonant interactions with ALPs, as illustrated in Figure 8 (bottom panel). As ν decreases over time, the function Eq.(D6) exhibits oscillatory behavior around zero. This oscillation is responsible for the similarly oscillatory pattern observed in φ_p , as it fluctuates around zero.

Finally, Figure 9 illustrates the phase difference in the orbital angle of a binary system when influenced by ALPs compared to a vacuum scenario. This phase difference shows how the dynamics of the binary system, affected by resonant forces from ALPs, result in a faster merger compared to vacuum scenarios.

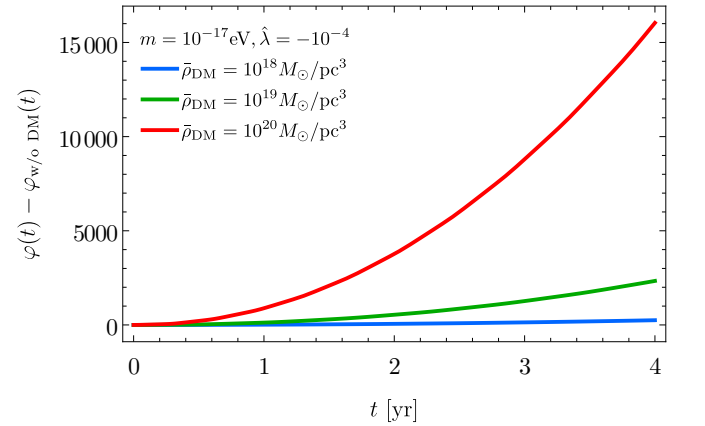


FIG. 9. The phase difference in the orbital angle of a binary system when influenced by ALPs compared to a vacuum scenario. The binary system and benchmark ALPs parameters are same as those presented in Figure 8.

-
- [1] G. Bertone and D. Hooper, *Rev. Mod. Phys.* **90**, 045002 (2018), arXiv:1605.04909 [astro-ph.CO].
 - [2] B. P. Abbott *et al.* (LIGO Scientific, Virgo), *Phys. Rev. Lett.* **116**, 061102 (2016), arXiv:1602.03837 [gr-qc].
 - [3] P. Amaro-Seoane *et al.* (LISA), (2017), arXiv:1702.00786 [astro-ph.IM].
 - [4] W.-H. Ruan, Z.-K. Guo, R.-G. Cai, and Y.-Z. Zhang, *Int. J. Mod. Phys. A* **35**, 2050075 (2020), arXiv:1807.09495 [gr-qc].
 - [5] J. Luo *et al.* (TianQin), *Class. Quant. Grav.* **33**, 035010 (2016), arXiv:1512.02076 [astro-ph.IM].
 - [6] N. Seto, S. Kawamura, and T. Nakamura, *Phys. Rev. Lett.* **87**, 221103 (2001), arXiv:astro-ph/0108011.
 - [7] R. D. Peccei and H. R. Quinn, *Phys. Rev. Lett.* **38**, 1440 (1977).
 - [8] R. D. Peccei and H. R. Quinn, *Phys. Rev. D* **16**, 1791 (1977).
 - [9] S. Weinberg, *Phys. Rev. Lett.* **40**, 223 (1978).
 - [10] F. Wilczek, *Phys. Rev. Lett.* **40**, 279 (1978).
 - [11] M. Demirtas, C. Long, L. McAllister, and M. Stillman, *JHEP* **04**, 138 (2020), arXiv:1808.01282 [hep-th].
 - [12] J. Halverson, C. Long, and P. Nath, *Phys. Rev. D* **96**,

- 056025 (2017), arXiv:1703.07779 [hep-ph].
- [13] M. Cicoli, M. Goodsell, and A. Ringwald, *JHEP* **10**, 146 (2012), arXiv:1206.0819 [hep-th].
- [14] B. S. Acharya, K. Bobkov, and P. Kumar, *JHEP* **11**, 105 (2010), arXiv:1004.5138 [hep-th].
- [15] A. Arvanitaki, S. Dimopoulos, S. Dubovsky, N. Kaloper, and J. March-Russell, *Phys. Rev. D* **81**, 123530 (2010), arXiv:0905.4720 [hep-th].
- [16] K.-S. Choi, H. P. Nilles, S. Ramos-Sanchez, and P. K. S. Vaudrevange, *Phys. Lett. B* **675**, 381 (2009), arXiv:0902.3070 [hep-th].
- [17] J. P. Conlon, *JHEP* **05**, 078 (2006), arXiv:hep-th/0602233.
- [18] P. Svrcek and E. Witten, *JHEP* **06**, 051 (2006), arXiv:hep-th/0605206.
- [19] E. Witten, *Phys. Lett. B* **149**, 351 (1984).
- [20] A. Arvanitaki and S. Dubovsky, *Phys. Rev. D* **83**, 044026 (2011), arXiv:1004.3558 [hep-th].
- [21] A. Arvanitaki, M. Baryakhtar, and X. Huang, *Phys. Rev. D* **91**, 084011 (2015), arXiv:1411.2263 [hep-ph].
- [22] A. Arvanitaki, M. Baryakhtar, S. Dimopoulos, S. Dubovsky, and R. Lasenby, *Phys. Rev. D* **95**, 043001 (2017), arXiv:1604.03958 [hep-ph].
- [23] M. Bošković, M. Koschnitzke, and R. A. Porto, (2024), arXiv:2403.02415 [gr-qc].
- [24] A. Hook and J. Huang, *JHEP* **06**, 036 (2018), arXiv:1708.08464 [hep-ph].
- [25] J. Huang, M. C. Johnson, L. Sagunski, M. Sakellariadou, and J. Zhang, *Phys. Rev. D* **99**, 063013 (2019), arXiv:1807.02133 [hep-ph].
- [26] A. Maselli, N. Franchini, L. Gualtieri, T. P. Sotiriou, S. Barsanti, and P. Pani, *Nature Astron.* **6**, 464 (2022), arXiv:2106.11325 [gr-qc].
- [27] K. Wang and Y. Zhong, *Phys. Rev. D* **108**, 123531 (2023), arXiv:2306.10732 [astro-ph.CO].
- [28] P. Brax, C. Burrage, J. A. R. Cembranos, and P. Valageas, (2024), arXiv:2402.04819 [astro-ph.CO].
- [29] K. Kadota, J. H. Kim, P. Ko, and X.-Y. Yang, *Phys. Rev. D* **109**, 015022 (2024), arXiv:2306.10828 [hep-ph].
- [30] H. Kim, A. Lenoci, I. Stomberg, and X. Xue, *Phys. Rev. D* **107**, 083005 (2023), arXiv:2212.07528 [astro-ph.GA].
- [31] A. Boudon, P. Brax, P. Valageas, and L. K. Wong, *Phys. Rev. D* **109**, 043504 (2024), arXiv:2305.18540 [astro-ph.CO].
- [32] C. F. B. Macedo, P. Pani, V. Cardoso, and L. C. B. Crispino, *Astrophys. J.* **774**, 48 (2013), arXiv:1302.2646 [gr-qc].
- [33] P. S. B. Dev, M. Lindner, and S. Ohmer, *Phys. Lett. B* **773**, 219 (2017), arXiv:1609.03939 [hep-ph].
- [34] D. Blas, D. López Nacir, and S. Sibiryakov, *Phys. Rev. D* **101**, 063016 (2020), arXiv:1910.08544 [gr-qc].
- [35] D. Blas, D. L. Nacir, and S. Sibiryakov, *Phys. Rev. Lett.* **118**, 261102 (2017), arXiv:1612.06789 [hep-ph].
- [36] M. Bošković, F. Duque, M. C. Ferreira, F. S. Miguel, and V. Cardoso, *Phys. Rev. D* **98**, 024037 (2018), arXiv:1806.07331 [gr-qc].
- [37] A. Boudon, P. Brax, and P. Valageas, *Phys. Rev. D* **106**, 043507 (2022), arXiv:2204.09401 [astro-ph.CO].
- [38] P. Brax, J. A. R. Cembranos, and P. Valageas, *Phys. Rev. D* **100**, 023526 (2019), arXiv:1906.00730 [astro-ph.CO].
- [39] B. Mashhoon, *Astrophysical Journal* **223**, 285 (1978).
- [40] E. Poisson and C. Will, *Gravity: Newtonian, Post-Newtonian, Relativistic* (Cambridge University Press, 2014).
- [41] M. Maggiore, *Gravitational Waves: Volume 1: Theory and Experiments*, Gravitational Waves (OUP Oxford, 2008).
- [42] N. Yunes, K. G. Arun, E. Berti, and C. M. Will, *Phys. Rev. D* **80**, 084001 (2009), [Erratum: *Phys. Rev. D* **89**, 109901 (2014)], arXiv:0906.0313 [gr-qc].
- [43] T. Robson, N. J. Cornish, and C. Liu, *Class. Quant. Grav.* **36**, 105011 (2019), arXiv:1803.01944 [astro-ph.HE].
- [44] L. J. Rubbo, N. J. Cornish, and O. Poujade, *Phys. Rev. D* **69**, 082003 (2004), arXiv:gr-qc/0311069.
- [45] C. Ünal, F. Pacucci, and A. Loeb, *JCAP* **05**, 007 (2021), arXiv:2012.12790 [hep-ph].
- [46] M. Baryakhtar, M. Galanis, R. Lasenby, and O. Simon, *Phys. Rev. D* **103**, 095019 (2021), arXiv:2011.11646 [hep-ph].
- [47] V. M. Mehta, M. Demirtas, C. Long, D. J. E. Marsh, L. McAllister, and M. J. Stott, *JCAP* **07**, 033 (2021), arXiv:2103.06812 [hep-th].
- [48] K. Blum, R. T. D’Agnolo, M. Lisanti, and B. R. Safdi, *Phys. Lett. B* **737**, 30 (2014), arXiv:1401.6460 [hep-ph].
- [49] J. Zhang, Z. Lyu, J. Huang, M. C. Johnson, L. Sagunski, M. Sakellariadou, and H. Yang, *Phys. Rev. Lett.* **127**, 161101 (2021), arXiv:2105.13963 [hep-ph].
- [50] C. O’Hare, “cajohare/axionlimits: Axionlimits,” <https://cajohare.github.io/AxionLimits/> (2020).
- [51] A. Arvanitaki, A. Madden, and K. Van Tilburg, *Phys. Rev. D* **109**, 072009 (2024), arXiv:2112.11466 [hep-ph].
- [52] D. F. Jackson Kimball *et al.*, *Springer Proc. Phys.* **245**, 105 (2020), arXiv:1711.08999 [physics.ins-det].
- [53] P.-H. Chavanis, *Phys. Rev. D* **84**, 043531 (2011), arXiv:1103.2050 [astro-ph.CO].
- [54] P. H. Chavanis and L. Delfini, *Phys. Rev. D* **84**, 043532 (2011), arXiv:1103.2054 [astro-ph.CO].
- [55] D. G. Levkov, A. G. Panin, and I. I. Tkachev, *Phys. Rev. Lett.* **118**, 011301 (2017), arXiv:1609.03611 [astro-ph.CO].
- [56] A. Khmel'nitsky and V. Rubakov, *JCAP* **02**, 019 (2014), arXiv:1309.5888 [astro-ph.CO].
- [57] G. Watson, *A Treatise on the Theory of Bessel Functions*, Cambridge Mathematical Library (Cambridge University Press, 1995).